ARTICLE

Growth Dynamics for DNA-Guided Nanoparticle Crystallization

Subas Dhakal,[†,§,⊥] Kevin L. Kohlstedt,[†,‡,⊥] George C. Schatz,[‡] Chad A. Mirkin,[†,‡] and Monica Olvera de la Cruz[†,‡,*]

[†]Department of Materials Science and Engineering and [‡]Department of Chemistry, Northwestern University, Evanston, Illinois 60208, United States. [⊥]These authors contributed equally to this work. [§]Present address: Department of Biomedical and Chemical Engineering, Syracuse University, Syracuse, New York 13244, United States.

ABSTRACT Spherical nucleic acid (SNA) nanostructures assemble into a large variety of well-defined crystalline superlattices *via* DNA-directed hybridization. Crystallities of SNA with various shapes emerge during the assembly process, which coalesce during coarsening, leading to polycrystalline materials. Here, we investigate the growth dynamics of SNAs into body-centered cubic superlattices and the coalescence of SNA aggregates using a colloidal model formulated from the competition of electrostatic core repulsions and localized DNA hybridization attractions. We find that the growth law of isolated SNA crystallities is well-described by the power law $t^{1/2}$, in agreement with experimental observations. At later times, coalescence slows the growth dynamics considerably and is dependent on the orientational mismatch (misorientation angle) of the coalescing crystallites. Molecular dynamics simulations show that the misorientation angle decreases continually during the coalescence, which is a signature of the grain rotation induced coalescence mechanism. This mechanism is followed by the coarsening of a "neck" that develops at the boundary between the coalescing crystallites. Remarkably, we find faster coalescence dynamics for larger SNAs compared to smaller SNAs due to their enhanced surface diffusion, which more effectively reduces curvature at the boundary of two superlattices. These findings provide fundamental insight into the relationship between nanoparticle surface chemistry and its crystallite growth and coalescence.

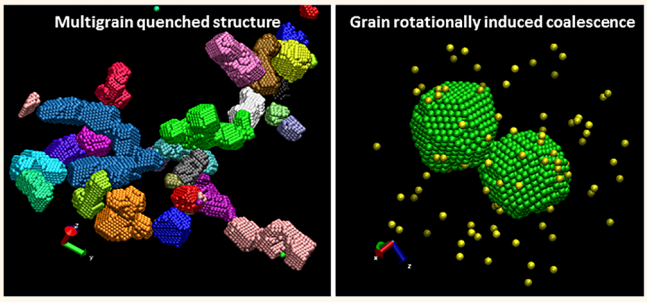

KEYWORDS: colloids · grain boundaries · nanoscale materials · DNA-functionalized · crystallization kinetics · synthons

Being able to functionalize nanoparticles with a wide variety of adsorbates has led to an unprecedented interest in colloidal crystals.[1−6] The large number of available nanoparticle sizes, shapes, and chemical functionalities has led to assemblies with distinct electrical,[7,8] optical,[9−14] magnetic,[15] and sensing properties[16] that are readily tunable *via* the chemistry of the building blocks. Spherical nucleic acid (SNA) nanostructures (nanoparticles with densely packed oligonucleotides spherically arranged on their surfaces) have emerged as a major building block in this area, due the structural and chemical control available with DNA linkers[17] leading to well-defined superlattice structures. A goal in the field is to create assemblies of nanoparticles with control over crystal lattice symmetry and spacing, as well as crystal shape and composition, recently seen with kinetically controlled superparticles.[18] The difficulties in realizing high-quality crystals resides in understanding how to control the coarsening and coalescence dynamics of crystallites comprised by DNA linkers. In SNA crystallization, it is difficult to form single crystals because annealing strategies have shown limited success in causing the coalescence of grain boundaries.[19] Indeed, understanding the role that DNA energetics and valency play in the dynamics of SNA coalescence is highly desirable. Previous experiments[4,5,20] and coarse-grained models[21−25] have investigated the stability of phase diagrams by changing the geometry[26] and binding potential of the SNA building block.[27] Here, we build upon these results to construct a colloidal model that quantitatively describes SNA superlattice growth dynamics and explain the role of grain boundaries during coalescence of two SNA crystallites.

The mechanical, transport, and melting properties of polycrystalline materials are determined not only by the chemical composition of the component crystals but also

* Address correspondence to m-olvera@northwestern.edu.

Received for review August 27, 2013 and accepted November 7, 2013..

Published online November 26, 2013
10.1021/nn404476f

by the size of the crystallites and the structure of the grain boundaries (GBs) that separate neighboring crystallites having different crystallographic orientation.[28−33] Grain boundary diffusion and coalescence are central to, and often, intertwined in crystal growth.[33,34] Using the colloidal interaction potential based upon short DNA binding regions, which bind to complementary DNA sequences *via* hybridization, we are able to perform molecular dynamics (MD) simulations to assemble crystalline aggregates and measure their growth dynamics, providing fundamental information on the coarsening and coalescence mechanisms.

In the initial stages, when the crystalline aggregates are isolated from each other, we find that the crystallite size a grows with time t, following the power law $a(t) \propto t^{1/2}$, in both our model and the experiments. Slow growth is observed when the crystallites coalesce due to the formation of a grain boundary at the interface. The formation of a GB subsequently leads to the coalescence time being dependent on the GB misorientation angle as well as the SNA size. We provide important details regarding the relationship between the orientation of the crystallites and the mechanism for crystal growth. Interestingly, we find large SNA nanoparticle sizes speed up the coalescence dynamics, suggesting that, besides bulk diffusion constants, the interaction length scales affect the crystal growth rate. We conclude with a discussion of the origin of this interplay between crystallite coalescence and SNA interaction length scales and provide insight into the factors that control the assembly of SNAs into large, uniform crystals.

RESULTS AND DISCUSSION

Interaction Potential. We begin by crafting a SNA colloidal model that captures both the highly localized charged environment and the polyvalent binding region of the SNA structure. We require the model to account for the experimental conditions of the SNA assembly such as high salt concentration, variable Au core sizes and DNA lengths, and flexible linker interactions. We first write the major contributions of the interparticle interaction arising from the duplex formation and electrostatic repulsion due to ion confinement. From this, two length scales emerge for the SNA system—a length scale $R = \sigma/2 + L$ corresponding to the size of the SNA including the Au core size σ and the DNA length L, and a second corresponding to the flexibility of the sticky ends l that binds nanoparticles together (see Figure 1). The interplay of these length scales with the interaction potential is nontrivial since the length of the DNA affects the local salt concentration,[24] the SNA radius R, linker density, and linker overlap volume.

Single SNAs in electrolyte solutions have been previously modeled using classical density functional theory (DFT).[24] The theory provides values for the high

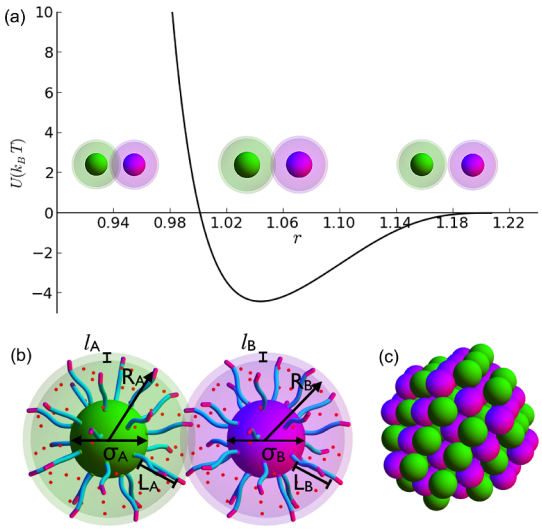

Figure 1. (a) Total potential U for a pair of SNA particles with $R_{A,B}$ = 14.3 nm, $l_{A,B}$ = 3.0 nm, and $\sigma_{A,B}$ = 10.0 nm. (b) Model colloidal SNA particles used as building blocks for aggregates. The DNA consists of a linker region (blue) and a terminal non-self-complementary sticky end (pink). The Au core diameter is σ, while the model SNA particle has a radius R. The flexible DNA strands lead to an overlap region of width l (light shade). (c) Typical body-centered cubic crystallite assembly seen in the simulations, which at equilibrium is a rhombic dodecahedron.

counterion concentration in the vicinity of the SNA nanoparticle. Molecular dynamics simulations further confirmed the high salt environment surrounding the dsDNA corona.[24] Here, we are primarily concerned with SNA assembly into colloidal crystallites composed of dsDNA linkers with terminal ssDNA linkers. This system has similarities to previous studies of the effective interaction between rigid dsDNA linkers,[35,36] but with much shorter unpaired ssDNA linkers, which lead to fast binding/unbinding rates.[37] Such fast kinetics may even allow rotational diffusion of the SNA.[38,39] We consider a binary SNA system of type A and B and disallow self-complementarity. The binding region is sufficiently far from the Au surface that excluded volume effects are indistinguishable (see Figure 1b). We employ a conceptually similar electrostatics treatment.[24] However, we do not modify the ion densities to account for ion−ion excluded volume effects since we are only interested in interactions between SNA at the terminal ends of the dsDNA linkers where ion concentrations are near bulk concentrations $\rho_i \sim \rho_i^{\infty}$. In this region, ion correlations are not likely to affect greatly the accuracy of the Poisson−Boltzmann (PB) theory, as would occur near the Au surface. Using the weak overlap limit, we can write the electrostatic potential Φ between two surfaces at a distance d as[40]

$$\Phi(d) = \int_d^{\infty} \Pi(r)\mathrm{d}r = \int_d^{\infty} \left[\sum_i \rho_i^{o}(r) - \sum_i \rho_i^{\infty}(r)\right]\mathrm{d}r \quad (1)$$

where Π is the electrolyte pressure (force) between the SNAs, and ρ_i^{o} and ρ_i^{∞} are the midplane ($d/2$) and bulk ion

densities for species i, respectively. Using the Derjaguin approximation, we can solve Φ in a planar geometry and transform it to a spherical geometry since $d \ll R$ (see Materials and Methods).[41] Solving eq 1 for a pair of SNAs with radii R_A and R_B, we write the electrostatic potential as

$$\Phi(d) = 128\pi\rho_\infty \bar{R}_{AB}\gamma^2 e^{-\kappa d} \quad (2)$$

where $\bar{R}_{AB} = R_A R_B/(R_A + R_B)$, κ is the inverse Debye length, ρ_∞ is the bulk ion concentration, and γ relates the strength of the effective surface potential ψ to the total potential Φ (see Materials and Methods section for values used). We note that eq 2 is written in units of κ^2/k_BT with $\kappa^2 = 4\pi\rho_\infty l_B$, where l_B is Bjerrum length.

The constituent DNA linker of the assembled SNA has configurational entropy. That is, they are not rigid rods, and the short binding regions at the ends of the linkers are not constrained to a fixed distance away from the NP surface. Instead, they have access to a range of distances that is a function of the rigidity of the linker and therefore contribute to the entropy of the SNA. Therefore, the SNA does *not* have a fixed radius over the region of size l (see Figure 1b). These overlapping regions are reminiscent of depletion regions between colloids embedded in a polymer solution.[42] The attractive potential "turns on" when adjacent SNAs have overlapping binding regions[35] or $d < 2R + l$ and is modulated by the amount of overlapping volume between a pair of SNAs

$$\Delta F = -k_B T n_{DNA}\left(\frac{\Delta V}{V}\right) \quad (3)$$

Here, the overlap volume between complementary SNA particles ΔV accounts for the polyvalent binding potential of the SNA linkers, and V is the SNA volume. In the limit of stiff dsDNA, the DNA surface coverage n_{DNA} of the SNA can easily be related to the DNA surface density,[4] while ΔV can be approximated as overlapping surface areas ΔA. Both ΔV and ΔA are related to the length of the dsDNA linker L and binding region size l, as shown in the Materials and Methods section. For small values of l ($l/R \sim 0.1$), the overlapping surfaces ($\Delta F \sim \Delta A$) potential should follow the body-centered cubic (bcc) superlattice kinetics trends found here using ΔV. We relate the overlap volume at a distance d to the attractive potential $F(d)$ as

$$F(d) = -\pi k_B T n_{DNA}\left(\frac{(v_a - v_b d + d^3)d - 3v_c}{12dV}\right) g(R) \quad (4)$$

where v_a, v_b, and v_c are SNA geometry-dependent constants (R_A,R_B,l_A,l_B). A Gaussian function $g(R)$ is employed to smoothly truncate the attractive potential at the cutoff distance (see Materials and Methods section). The total pair interaction potential $U(d)$ is written as the sum of the (scaled) electrostatic repulsion due to electrolyte screening Φ' and the linker attraction $F(d)$

$$U(d) = \Phi'(d) + F(d) \quad (5)$$

with $\Phi'(d) = \Phi(d)k_BT/\kappa^2$. $U(d)$ governs the dynamics in our molecular dynamics simulations.

TABLE 1. SNA Parameters in the Simulations

R (nm)	σ/L	l (nm)	R (nm)	σ/L	l (nm)
12.3	3.1	3.0	17.9	2.58	4.8
14.3	1.86	3.0	21.5	3.30	6.0
16.3	1.32	3.0	26.6	4.32	7.7
18.3	1.03	3.0	33.2	5.64	9.9
20.3	0.84	3.0			

Isolated SNA Crystal Growth. Before we investigate the growth of multiple interacting crystallites, we first investigate the growth of isolated SNA crystallites and, subsequently, compare their growth dynamics with recent experimental measurements.[19] We focus on SNA sizes that are consistent with bcc lattice formation. We choose a binary system where $R_A = R_B$ and $l_A = l_B$ for simplicity and analyze different ratios σ/L to determine the effect of the relative length of the DNA to the diameter of the Au-NP in the coarsening dynamics. We summarize our SNA geometry parameters in Table 1.

The size of individual crystallites ranges from 100 nm to 4 μm in the simulations. For SNA concentrations of ~10 nM, the simulation crystallite sizes agree well with available experiments.[4] In all of the simulations presented in this paper, the system is started at a temperature well above the melting or disordering temperature, T_m, and slowly cooled at the rate of 10^{-5} °C τ^{-1}. The location of the melting temperature is determined by tracking the SNA separation d from the position of the peaks of the SNA radial distribution function. We find the onset of crystallization with the formation of a sharp Bragg peak below T_m consistent with the bcc lattice by using small increments of the rescaled temperature $\Delta T = 0.01$. For completeness, we evaluate the bond-order parameter Q_6 that quantifies the degree of crystalline order;[43] Q_6 shows a discontinuity at the transition from the liquid state to the crystalline state at T_m (see the Supporting Information).

We confirm that the SNA spacing d scales linearly with R, as shown in Figure 2a, and that the spacing d compares favorably with SAXS data for SNA bcc crystals.[4] Since the stability of the crystals changes for different SNA sizes, we show T_m as a function of the SNA radius R and the width of the overlap region l in Figure 2. We find that decreasing the Au/DNA ratio σ/L increases the thermal stability of the lattice.[4,44] This is expected since in our model small σ/L values translate into large overlapping volumes for the linkers and, therefore, in an increase of the binding energy between neighbors. In contrast, large σ/L values generate shallow binding potentials (*i.e.*, small overlapping

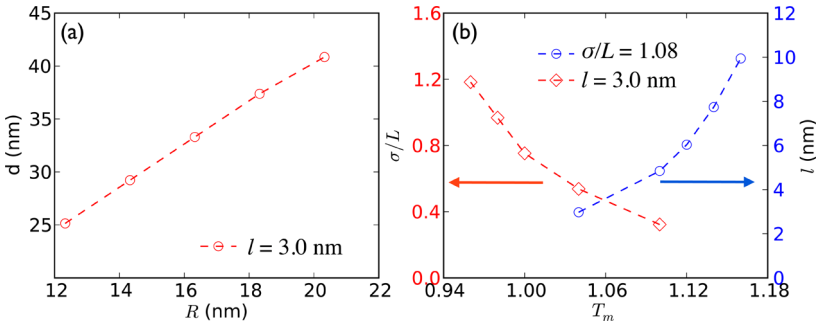

Figure 2. (a) SNA separation *d* scales linearly with increasing NP core sizes σ. The DNA lengths are fixed to L = 9.3 nm and l = 3.0 nm. (b) SNA melting temperatures T_m are shown independently as a function of (i) σ/L for a fixed l = 3.0 nm and L = 9.3 nm (◇), and (ii) l for a fixed NP core size σ = 10.0 nm (○).

linker regions), which leads to a low melting temperature, as shown in Figure 2b. All of the structural and dynamical properties reported in this paper are near the onset of the melting transition; that is, we set $T \approx 0.96T_m$, which allows kinetically unfavorable states to be annealed.

During coarsening, the diffusion equation under steady-state conditions for a constant bulk diffusion D, $D\nabla^2 c = 0$ can be solved for spherically symmetric nuclei.[45] At early times, when the bulk SNA concentration is time-independent, the nuclei size $a(t)$ growth rate is given by[46]

$$a(t) = \sqrt{2sDt} \tag{6}$$

where D is the bulk diffusivity and s is a constant determined by the supersaturation driving force. The number concentration of crystallites N_G is given by

$$N_G(t) = \frac{3}{4}\pi(2s^{1/3}Dt)^{-3/2} \tag{7}$$

In addition to the diffusion parameters required to determine the nucleation and growth process of spherical nuclei, the growth models of anisotropic nuclei require the growth velocities of the different crystal planes.[47,48] The shapes of the bcc superlattice grains are not isotropic since the unit cells are not isotropic. In equilibrium, the crystal shapes are generally determined by the Wulff construction method,[49] which leads to regular polyhedral crystal shapes. In our MD simulations, we observe faceted shapes, which are kinetic shapes and are studied by crystal growth using anisotropic growth models.[47,48] Our aim is not to classify the kinetic shapes. Instead, our goal is to relate the SNA colloid model parameters to the SNA crystallite kinetics to determine the model range of validity by comparing our results to experiments.

We begin by distinguishing the SNAs based on their local environment within each crystallite, making a direct measurement of the interface kinetics possible, and subsequent comparison of the growth dynamics of the different environments. SNAs that are freely diffusing in the bulk are designated as type **b** (background SNAs). Type **s** surface SNAs are defined as the interfacial SNAs that are within $d < 2R$ of the crystallite. We further classify two types of SNAs within the crystallite as type **bs**, which are just below the interface, within a distance $2R$ below the surface, and type **c**, which are crystalline SNAs, with a coordination number of 8 nearest neighbors. The different types of SNAs are distinguished with a color scheme in Figure 3b (type **b**, yellow; type **s**, green; type **bs**, purple; type **c**, orange).

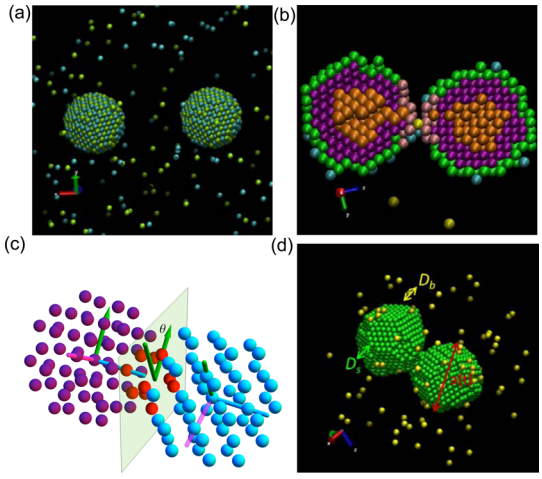

Figure 3. (a) Typical initial configuration used to study the coalescence of bcc crystallites of size $a(t = 0)$ = 143 nm. (b) We classify the SNA in the system based on coordination number: Type b are bulk SNA (yellow); type s are surface SNA (green); type sb are SNA within distance $2R$ below the surface (violet), and type c are crystalline SNA (orange). (c) Diagram of two crystallites from (a) with misorientation angle θ defined at the interfacial plane or grain boundary (green shade). Red SNAs are those lying at the grain boundary. The arrows represent the lattice orientation of an individual crystallite. For clarity, each SNA crystallite is distinctly colored (left purple and right cyan). (d) We classify two types of SNA diffusion based on coordination number—surface SNAs have diffusivity D_s and bulk SNA D_b.

At low SNA concentrations, ~10 nM, the crystallite growth is initially not impinged by collisions between nuclei. In Figure 4a, we show the time evolution of the crystallite size $a(t/\tau)$, where τ is the characteristic simulation time $\tau \approx 10$ ps for SNA size R = 12.3 nm and DNA length L = 9.3 nm. We find three distinct

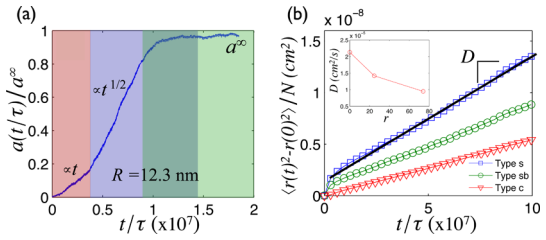

Figure 4. (a) Normalized crystallite size $a(\tau)$ in a single-crystal growth as functions of time for R = 12.3 nm SNA. The growth falls into three regimes: first-order linear (pink), diffusive parabolic (blue), and a crossover region with a decaying concentration a^{∞} (blue-green). The arrested growth is shown as a^{∞}, the final crystal size (green). (b) Mean square displacements during growth for an isolated crystallite for three types of SNA—types s, sb, and c with filled squares, circles, and triangles, respectively. At the diffusive region, the slope of the each SNA msd (D) is plotted in the inset. The inset shows D as a function of distance from the surface of a single crystal toward the center.

growth regions with two that are well-described by power laws. Region I (pink shade in Figure 4a) shows $a(t/\tau)$ during nucleation growing linearly with time, which follows predictions based on first-order interfacial kinetics $da(t/\tau) = k(T_I - T)dt$,[45] where $T_I = T_m - \Gamma/a$ is the temperature of the growing interface and is dependent on the Gibbs−Thomson coefficient Γ and the surface curvature $1/a$. The linear scaling $a \propto t$ is based on a small amount of supersaturation (in our simulations, we keep $T = 0.96T_m$). Regime II (blue shade) shows a slower, nearly parabolic growth $a^2 \propto t$, which is discussed below. The actual measured growth rate in region II fits to $a(t/\tau) = a_0(t/\tau)^{0.47\pm0.05}$, as shown in Figure 4a. We observe a crossover slow growth region, shown in a mixed green-blue shade in Figure 4a, before $t \rightarrow \infty$, when the supersaturation driving force decays to zero and growth stops, $a(t \rightarrow \infty) \equiv a^{\infty}$ (green shade). To show the decay of the diffusivities from the equilibrated nucleus surface to its interior, we plot in Figure 4b the mean square displacement (msd) for types **s**, **sb**, and **c** SNAs. The corresponding diffusivities D are shown in the Figure 4b inset. The diffusion coefficient of SNAs at the interface D_s is a factor of 2 larger than the SNAs just below the surface. In the next section, we analyze the competition of surface diffusion *versus* bulk diffusion to determine the coalescence dynamics mechanism.

Coalescence Dynamics. At times longer than the mean-free coalescence time, τ_m, growth no longer occurs in an isolated matrix. Coalescence further coarsens the crystallites. In the dilute limit, the majority of crystallite coalescence is pairwise, and we consider the SNA crystallite growth in this limit. In order to track the dynamics of crystallites during coalescence, we first consider a large system with 40−50 crystallites that nucleate upon supercooling a gas (an implicit solvent) of SNA to $T = 0.96T_m$. Figure 5a,b shows a representative snapshot of the crystallite configuration for a large system ($N = 4 \times 10^4$ SNA) exhibiting the characteristic polycrystallinity of bcc crystallites found experimentally[4] and in our simulations, respectively. We track the coarsening rate using two well-studied metrics, grain (crystallite) density N_G and crystallite size $a(t/\tau)$. For the quenches near the melting temperature studied here, the crystallites are rarefied and the distance between them is large, that is, $\lambda \equiv c(0)^{-1/3} \ll a(0)$, where $c(0)$ is the initial concentration of the nucleated particles and $a(0)$ is the size of the spherical nucleus at $t = 0$. A typical initial concentration of SNA particles is 10 nM, which leads to a $\lambda \sim 550$ nm while $a(0) \sim 50$ nm.

Using cluster analysis and particle tracking, we calculate N_G over a series of trajectories, and we show them for $R = 14.3$ nm in Figure 5c, which is comparable to the experimental SNA value, $R = 15$ nm. Additionally, we plot the experimental crystallite density from ref 19 for bcc crystallite growth in Figure 5c. Interestingly, we find that the data in the simulations and experiment only at very early times $t/\tau < 2$ vaguely resemble the predicted growth of spherical nuclei in eq 7 (dashed line in Figure 5c). Both the experimental and simulation data show a slower decay at longer times, which seems to evolve to the classical Ostwald ripening regime ($N_G \propto 1/\tau$). This, however, may be due to the anisotropic growth rates of the faceted crystal. Other complications arise due to the overlap of nuclei diffusion zones altering the constant supersaturation driving flux that is used in the theory.[45] This overlap causes depletion zones and lowers the driving force, which may also explain the slow decay we find in Figure 5c. We also calculate $a(t/\tau)$ during coarsening in Figure 5d. Unexpectedly, $a(t/\tau)$ follows the predicted quadratic growth of eq 6, $t^{1/2}$ not only at early times ($t/\tau < 2$) but also at longer times, in agreement with the experimental data. That is, we do not find the classical Ostwald ripening regime $a \propto t^{1/3}$. The latter stage time growth correspondence of $a(t)$ between the MD simulations and the experimental results shows that the SNA colloid model does well to approximate the crystallite kinetic growth mechanism.

Previous studies have shown the interplay between the dynamics of crystallite coalescence and the growth rate (*e.g.*, $da(t)/dt$) in polycrystalline materials.[51] The driving force for the coalescence of crystallites, however, is the minimization of the surface energy by elimination of interfaces, grain boundaries, and defects which proceed through the volume, surface, and grain boundary diffusion.[52] Therefore, understanding the individual colloidal scale diffusion is a prerequisite to a comprehensive description of the crystal growth in polycrystalline materials. As a first step to understand the grain boundary diffusion in bcc crystallites, we perform a number of simulations starting from a pair of equilibrated crystallites of size $a_0 \equiv a(t = 0)$ with background SNA concentration of 2% by volume fraction using the same interaction potential given in eq 4. We then prepare the MD simulation by inserting the crystallites at a distance of $4a_0$, as shown in Figure 3a.

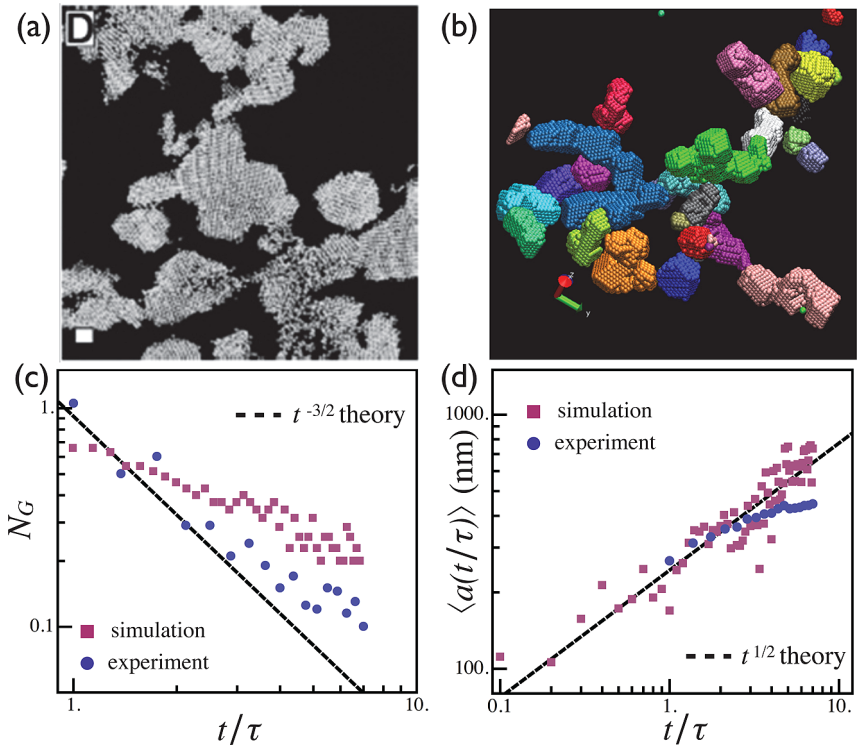

Figure 5. (a) TEM image of a bcc crystallite in recent SNA experiments.[4] The scale bar represents 200 nm. (b) Snapshot of a bcc crystallite in simulations. Simulation snapshots are generated with the Visual Molecular Dynamics package.[50] The individual crystallite size ranges from 100 nm to 4 μm. (c,d) Number of crystallites N_G and the average crystallite size $\langle a(t/\tau)\rangle$ as a function of time are plotted from the model (red squares) and experiments (blue disks) from ref 19. In panel (d), the simulation data are shifted vertically down by 700 nm for comparison. Theory predictions from eqs 6 and 7 are shown as dashed lines. These simulations, similar to the experiments, correspond to $R = 14.3$ nm, $L = 9.3$ nm, and $l = 3.0$ nm; we set $T = 0.96T_m$ in our model.

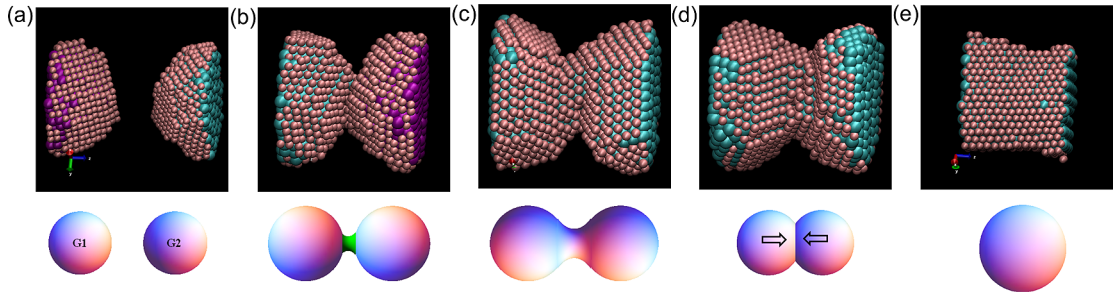

Figure 6. Top row: Temporal evolution of the crystallites during coalescence in simulations. Bottom row: Proposed mechanism of crystallite coalescence for bcc crystallites. (a) Initial state. (b) Grain boundary development. (c) Grain boundary diffusion and development of a neck. (d) Diffusion-limited neck growth. (e) Final stage for an ideal system. However, the final configurations in simulations are faceted.

These simulations provide a unique opportunity for the direct measurement of different time scales involved in the crystal growth. By limiting the coalescence to a pair of crystallites, we disallow any triple junctions or impingement effects. We found that in our polycrystalline simulations as well as in experimental growth (Figure 5a,b) triple junctions are very rare in these systems for moderate crystallite sizes; for the analysis of the coalescence of pairs of crystallites, we limit here to a_0 less than 250 nm (we have evidence of triple junction only when $a_0 > 1-4$ μm).

We show the time evolution of the coalescence with snapshots from the MD simulations in Figure 6, and we guide the reader with a schematic of the crystallite coalescence below the snapshots. We find that the orientation of the two crystallites is a key determinant of the coalescence dynamics. Depending upon the angle of approach, a grain boundary between two crystallites develops. To minimize the costly interfacial energy, the crystallites undergo rotations or reorientation until the crystallites assume a homogeneous orientation; see top panel of Figure 6a–c. After complete elimination of the GB, a neck develops, which consists of a bridge of crystalline SNAs connecting the crystallites with concave curvature at the center of the neck, while the crystallite surface has convex curvature.

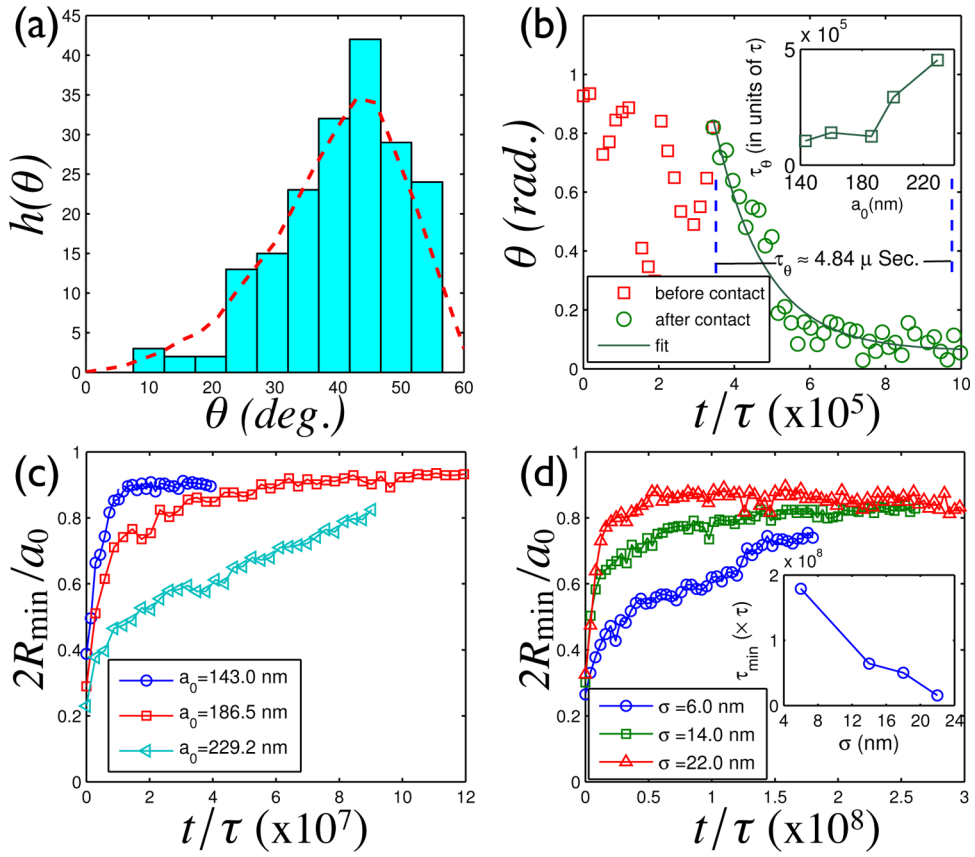

Figure 7. (a) Histogram illustrating the distribution of misorientation angle for two bcc crystallites during the coalescence. The angle distribution is a left skewed normal distribution peaked at $\theta \approx 45°$. The Mackenzie distribution is overlaid with a red dash. (b) GB misorientation angle (θ) is plotted as a function of time for a pair of crystallites with $a_0 = 229.2$ nm. The inset shows the dependence of τ_θ during the coalescence of two bcc crystallites with initial diameters $a_1 = a_2 = a_0$ nm. (c) Simulation results showing the evolution of neck radius as functions of time for a pair of crystallites ($R = 14.3$ nm, $L = 9.3$ nm, and $l = 3.0$ nm) starting from three crystallite sizes. (d) R_{min} as a function of time is shown for three different σ with $L = 9.3$ nm and $l = 3.0$ nm. Inset plot of τ_{min} as a function of σ.

The elimination of the two curvatures associated with the neck is the energetic driving force for coalescence and offers a simple minimal surface analysis *via* a two-sphere model of crystallite coalescence.[52] In the later stage of the coalescence, in an attempt to minimize the surface-to-volume ratio, or the surface energy γ, the neck coarsens and the final aggregate assumes a polyhedral shape. The dynamics of crystallite coalescence are therefore naturally separated into two time scales: (i) a time scale describing crystallite rotation due to the GB misorientation (τ_θ) and (ii) a time scale related to the growth of the neck (τ_{min}).

It is convenient to write the misorientation of the grain boundary as the rotation of an angle θ to bring crystallite A into coincidence with crystallite B when twist boundaries dominate (see Figure 3c and the Materials and Methods section for the calculation of θ]. To determine the distribution of this misorientation angle $h(\theta)$ between the crystallites, we repeat the simulations starting from different initial configurations at a fixed concentration. Figure 7a shows $h(\theta)$ for the SNA geometry with $R = 14.3$ nm, $L = 9.3$ nm, and $l = 3.0$ nm. These simulations show that the grain boundaries in bcc crystallites are dominated by high-angle grain boundaries ($\approx$45°) and follow the Mackenzie distribution[53] for random polycrystalline samples. Though there may be other dislocations besides twists that contribute to the grain boundary, their strain energies scale with the volume of the crystallites $\sim a^3$, and they tend to be eliminated during coarsening. We have performed a number of simulations with increasing σ, and the distribution of misorientation angle shows no significant dependence on σ, which is a signature for GBs that have Mackenzie distributions.[53] This suggests that the crystallites expose only one crystal plane to their surfaces; in equilibrium, the crystallite shape of a bcc superlattice is a rhombic dodecahedron, which seems consistent with the shape we find in the simulation during coarsening.

To better understand the coalescence dynamics of two crystallites, we investigated the relaxation of θ during coalescence. It is important to note that the coalescing crystallites undergo a continuous rotation until they have acquired the same orientation or $\theta = 0$ shown in Figure 7b with the plot θ *versus* t. The simulation results are consistent with the GB rotation

mechanism known as grain rotation induced coalescence (GRIC) found in metallic systems.[54,55] That is, the GB coalescence shows a strong dependence on θ in Figure 7b instead of only an Ostwald ripening mechanism, where the bigger crystallite starts growing at the expense of the smaller crystallites. The GRIC mechanism has been observed in both theory[56] and experiment.[54,55] To find the size dependence of the GRIC mechanism, simulations using $R = 14.3$ nm, $L = 9.3$ nm, and $l = 3.0$ nm are run by varying the initial crystallite size (a_0). We find that the grain boundary elimination for large crystallites is slow due to the larger rotational inertia, while for small crystallites ($a_0 < 180$ nm), τ_θ varies slowly with the initial grain size (a_0). This is reasonable as in the GRIC mechanism a large number of bonds between the SNAs have to be broken during the rotation. It can be inferred from the inset (see Figure 7b) that the GB persists over several microseconds upon increasing the grain size beyond 300 nm.

We further examine the GRIC mechanism by tracking the neck radius R_{min} for different a_0 as well as SNA sizes R. In order to make meaningful comparisons between different simulation runs, we integrate over the misorientation $h(\theta)$ for each neck size measurement. This ensures that we account for different misorientation angles while comparing the neck relaxation. The results are shown in Figure 7c,d, where the scaled neck radius ($2R_{min}/a_0$) is plotted as a function of time. From these calculations, we find that τ_{min} increases with the crystallite size for fixed SNA geometry R and l seen in Figure 7c. It is important to note that our simulations correspond to equal crystallite sizes, while in the experiments, and as also indicated by the simulations in Figure 5, there is a distribution of crystallite sizes in the SNA polycrystals. The polydispersity of sizes is ignored here to extract information on the surface that develops during neck growth in large crystallites. For example, by computing the scaled distance from the centers of the coalescing crystallites as a function of time, we find that a catenoid shape develops (see Supporting Information), which is a minimal surface present in many systems with sharp interfaces connecting regions of different curvature.[57,58]

We demonstrate the effect of R on the dynamics of crystallite coalescence by systematically varying the size of nanoparticles with fixed l and σ/L in the simulations. As described previously, the initial configuration is two equally sized crystallites at a fixed SNA background concentration. We track the coalescence of the crystallites and measure the neck radius ($2R_{min}/a_0$). We extract the neck growth time τ_{min} as functions of SNA size (R) (see Materials and Methods section). Figure 7d shows τ_{min} as a function of R. The inset provides clear evidence that large SNAs reduce the coalescence time τ_{min}. The reduction in coalescence time τ_{min} of the crystallites with increased core sizes could be due to the different diffusion mechanism (*i.e.*, bulk and surface diffusion) involved in SNA coalescence. We gain further insight into the coalescence dynamics by analyzing the msd of SNA in the **b** and **s** environments, shown in Figure 8 of the Supporting Information. We calculate the ratio of the diffusion constant (calculated from the msd) for surface SNA and the SNA near the surface in the bulk. To this end, we generalize Fick's law by assuming isotropic diffusion in all directions despite the fact that the diffusion is to some extent influenced by the curvature of the neck developed during coalescence. In its simplest form, the net flux away from the surface is

TABLE 2. Surface Diffusivities for Increasing SNA Radii

system ($L = 9.3$ nm, $l = 3.0$ nm)	D_s/D_b (%)
$R = 12.3$ nm	1.5
$R = 16.3$ nm	1.8
$R = 20.3$ nm	2.3

$$J \sim -\left(D_s \frac{\delta \phi_s}{\delta r} - D_b \frac{\delta \phi_b}{\delta r}\right)$$

where φ_s and φ_b are the number density of surface and bulk SNAs, respectively. In this dual diffusion limit, the ratio D_s/D_b provides a quantitative measure of the coalescence dynamics and can be used as a design principle for experimentalists. The ratio of the surface diffusion (D_s) to the bulk diffusion (D_b) as a function of R in Table 2 shows that surface diffusion stabilizes crystallites of SNAs with large R values. This demonstrates that R strongly affects the surface energy γ of the GB with larger R decreasing γ therefore decreasing the crystallite growth dynamics.

CONCLUSION AND OUTLOOK

In summary, we have developed a colloid model that captures the electrostatic repulsion of DNA-functionalized nanoparticles (SNA) as well as the energetic length scales of the DNA binding. We use the model to do molecular dynamics simulations that characterize the assembly of SNA nanoparticles into bcc crystallites. Using cluster tracking algorithms, we are able to track the growth of crystallites and their coarsening. We find that the size of isolated aggregates scales with a power law in time $a(t) \propto t^{1/2}$. At longer times, crystallite coalescence slows the dynamics. We further use the model to study the coalescence of two freely diffusing crystallites and confirm the grain rotation induced coalescence (GRIC) mechanism for the crystal growth during coalescence. With the help of the GRIC model, we find that two time scales describe the coalescence dynamics: the misorientation decay constant, τ_θ, and the minimal surface diffusion time, τ_{min}. Using these two time scales, we decouple the kinetics between GB rotation and the reduction of the surface curvature

during coalescence. The results from the GRIC mechanism reveal simple design rules for experimentalists to increase the crystallite size of crystals. First, large SNA nanoparticles facilitate crystal growth because the surface diffusion of larger SNAs is faster than smaller SNA nanoparticles. However, one must also consider that increasing R (for fixed dsDNA length L and linker length l) decreases the stability of the crystallite (Figure 2b). We show that this can be overcome by increasing the overlap volume ΔV the DNA linker has access to, which tends to increase the melting temperature T_m. Interestingly, this interplay between ΔV and the crystallite stability becomes ill-defined when $\Delta V \rightarrow 0$ (*e.g.*, for short linker regions or stiff DNA) due to the potential becoming purely repulsive. The binding is now effectively constrained to a surface, and in such cases, a transition must be made to overlapping surface areas ΔA. We note that similar crystal shapes for bcc systems have been obtained using ΔA,[59] and we expect ΔA and ΔV to be qualitatively similar.

In the classical view, Kramer's rule relates the diffusion process to the probability of overcoming an energetic barrier U as $D = \text{const.} \times e^{-U/k_B T}$. The barrier in our model is an electrostatic repulsion screened by the ion cloud around the SNA, which at high salt concentrations can be computed using instead a hard core repulsion that prevents SNA overlap at distances less than $2R$ due to the high density of ions required to cancel the charge of the dsDNA grafted to the gold nanoparticles. We note that, as in our linearized electrostatic model, this hard core repulsion decays to zero over short distances away from the SNA surface at high salt environments ($\kappa R \gg 1$).[24] Therefore, the results of our model are robust and could be applied to a variety of systems with competing repulsive and attractive short-range ($d \ll R$) forces. We conclude that there are optimal values of nanoparticle size R and DNA linker size l that lead to larger single-crystal crystallites. We hope that the insight here will stimulate a renewed discussion on the dynamics of crystallites in the SNA system both theoretically and experimentally.

MATERIALS AND METHODS

We used the LAMMPS[60] molecular dynamics package to simulate the crystallites. In each simulation, the initial configuration is prepared as follows. First, a random configuration of nanoparticles at a desired density is generated using the packmol software.[61] We further relax the system using a conjugate gradient minimization routine. The equation of motion is integrated for a constant NVT ensemble with the temperature controlled *via* a Nosé-Hoover thermostat. The time step in our simulation is $\Delta t = 0.002\,\tau$ in the units of $\tau = (m\sigma^2/\varepsilon)^{1/2}$, where m is the mass of a $R = \sigma/2 + L$ SNA, and the well depth is determined by the electrostatic repulsion and DNA attraction $\varepsilon \approx 3-5k_BT$. As an example, for $\sigma = 6.0$ nm and $L = 9.3$ nm system, $m = 8.32 \times 10^{-22}$ kg, and a unit time step corresponds to $\tau = 11.27$ ps. Therefore, it is possible to study large systems on a long time scale at reasonable computational cost.

Model Interaction. Here, we provide a derivation of the electrostatic repulsion between the SNA in a monovalent electrolyte solution. We begin by relating the chemical potential μ_i of electrolyte species i to the force (per area) f under isothermal conditions by expanding the variational with respect to density

$$\frac{\partial f}{\partial \rho_i} = \rho_i \frac{\partial \mu_i}{\partial \rho_i} \tag{8}$$

Due to symmetry of the system, the density is only a function of the center-to-center distance of the SNA, and eq 8 can be expanded in terms of the distance as

$$\frac{\partial f}{\partial r}\Big|_{r=d,T} = \rho_i \frac{\partial \mu_i}{\partial r}\Big|_{r=d,T} \tag{9}$$

For densely covered Au-NPs, it is safe to assume the concentration profile of the ions follows the Boltzmann distribution. Further, due to the radial nature of SNA particles, the concentration of DNA near the linker is small. The small DNA concentration at the SNA surface (not Au surface (see Figure 1) gives rise to weak effective surface potentials ψ that are much smaller than that at the Au-NP surface. Therefore, we simply sum the electrostatic interaction potential and entropic contributions to the chemical potential as $\mu_i = qi\Psi + kT\log\rho_i$. The potential is related to concentration *via* the Poisson equation $\nabla^2\psi = -q_i\rho_i/\varepsilon$. We can write the force for two infinite flat plates at a distance D from eq 8[40]

$$f(\infty) - f(D) = \sum_i k_B T \rho_i^{\infty} - \frac{1}{2}\varepsilon(\nabla\psi)^2\Big|_{\infty} + \frac{1}{2}\varepsilon(\nabla\psi)^2\Big|_{D} \tag{10}$$

with ρ_i^{∞} being the bulk concentration of electrolyte, ε the relative dielectric of the solvent, and the origin is taken to be at $D/2$ during the integration. The electrostatic force must decay to zero at $r \rightarrow \infty$ so $f(\infty) = 0$. We now take advantage of the symmetry of the origin lying at the midplane that allows us to relate the electrolyte density at the origin to that at the surface as

$$\sum_i \rho_i = \sum_i \rho_i^{o} + \frac{\varepsilon}{2kT}(\nabla\psi)^2 \tag{11}$$

where ρ_i^{o} is the density at the midplane defined as $\rho_i^{o} \equiv \rho_i(0) = \rho_i^{\infty} e^{-q\Psi_o/kT}$. Upon replacing eq 11 into eq 10, we see that the electrostatic potential terms cancel and we are left with only the force due to the pressure Π of the electrolyte between the SNA particles defined as

$$\Pi(D) = k_B T[\sum_i \rho_i^{o}(D) - \sum_i \rho_i^{o}(\infty)] = kT[\sum_i e^{-q_i\psi_o/kT} - \sum_i \rho_i^{\infty}] \tag{12}$$

We now restrict the calculation to a monovalent electrolyte and assume $\psi_o/kT < 1$, which assumes that $D > \kappa^{-1}$. We note that for shorter linker DNA sequences this approximation will break down and a modified Poisson–Boltzmann treatment will be needed. We write the electrolyte pressure to second-order as

$$\Pi(D) = \frac{16k_B T\gamma^2\kappa^2}{\pi l_B} e^{-\kappa D} \tag{13}$$

where $\gamma = \tanh(q\psi_s/4k_BT)$ modulates Π between 0 and the Debye–Hückel limit ($\rho_\infty e^{-\kappa D}$) *via* the strength of the surface potential ψ_s for the SNA particle and l_B expresses the length at which the strength of the electrostatic repulsion is equal to the thermal energy. For $\psi_s < 25$ mV, γ is essentially directly proportional to ψ_s. Above 150 mM NaCl concentrations, SNAs have most of the DNA core screened and we take $\gamma = 0.2$, which gives $\kappa = 1.27$ nm^{-1} and $l_B = 1.1$ nm. Finally, we utilize the Derjaguin approximation that relates any power law pairwise force between two spheres linearly to the potential between two infinite plates provided $D \ll R$ as[41]

$$\Pi_{SNA} = 2\pi \frac{R_A R_B}{R_A + R_B} \Phi_{plate} \quad (14)$$

with $\nabla\Phi_{plate} = -\Pi$.

The SNA attraction due to complementary DNA base hybridization is modeled as a spherically symmetric "sticky" potential modulated by the length of the linker ssDNA sequence *l*. We account for the SNA polyvalency by allowing multiple linker strands from adjacent SNA particles to bind. This can be modeled by an effective overlap volume ΔV between adjacent SNA particles. It is known that the dsDNA spacer in SNA particles shows a rise per base pair z_{ds} shorter than traditional B-form duplexes, and it is dependent upon the SNA geometry. This leads to the linkers having variable length from the surface of the Au-NP. For small Au-NP, $\sigma < 15$ nm, the measured rise per base pair is $z_{ds} = 0.255$ base/nm. We take that to the minimum energy distance of the linker and $z_{ds} = 0.34$ base/nm (B-form) as the maximum distance allowed. The linkers now occupy a spherical shell around the SNA, and when two SNA shells overlap, we calculate the ΔV using standard spherical overlap calculations. The attractiveness of the overlap potential is controlled by the DNA surface coverage n_{DNA} as shown in eq 3. We write the overlap volume for two spherical shells as

$$\Delta V = \frac{1}{3}\pi h^2(3R - h) \quad (15)$$

where *h* is the height of the spherical cap and *R* is the radius of the cap. Expanding eq 15 for two SNA, with radii R_A and R_B and linker extensions l_A and l_B, we rewrite the overlap volume as

$$\Delta V = \pi \frac{(v_A - v_B d + d^3)d - 3v_C}{12d} \quad (16)$$

The geometric constants are $v_A = 6c_C + 2c_B^3$, $v_B = 3c_A$, and $v_C = c_B c_C$, where $c_A = (R_A - R_B)^2 + (l_A + l_B + R_A + R_B)^2$, $c_B = l_A + l_B + R_A + R_B$, and $c_C = (R_A - R_B)^2 c_B$. We expect for short dsDNA spacer strands and dense surface coverages that ΔV can be approximated as an overlap area ΔA since the dsDNA spacer would be inextensible.[4] Using the ΔA expression from ref 4 and substituting for two SNAs, we get $\Delta A = \pi((c_A - c_B d)d - c_C)/d$. We note that both ΔA and ΔV reduce to a linear dependence of *d* when $R = R_A = R_B$ and $d \ll R$. Finally, we smooth the transition of the overlap potential at the maximum linker d_{max} distance with a Gaussian smoothing function $G(d) = (1 - e^{-\eta(d-d_{max})^2})$, where $\eta \sim 10^{-3}$ is a small parameter controlling the width of the smoothing. This ensures the force goes to zero continuously.

Grain Boundary Classification. The local orientation of a crystal lattice is determined from the position vectors to the six second-nearest-neighbors in bcc lattice. Out of the six vectors, the three distinct vectors constitute the orientation of the crystallites in the laboratory frame. In a cubic polycrystalline material, the orientation between two crystallites labeled A and B with orientation g^A and g^B can also be represented by a matrix $g = g^A g^{-B}$, with the local orientation of each crystallite described by a set of vector triads $g = (n,b,c)$ or by a set of Euler's angles (θ, φ, ψ). The rotation matrix is

$$g = \begin{pmatrix} \hat{n}_A \cdot \hat{n}_B & \hat{n}_A \cdot \hat{b}_B & \hat{n}_A \cdot \hat{c}_B \\ \hat{b}_A \cdot \hat{n}_B & \hat{b}_A \cdot \hat{b}_B & \hat{b}_A \cdot \hat{c}_B \\ \hat{c}_A \cdot \hat{n}_B & \hat{c}_A \cdot \hat{b}_B & \hat{c}_A \cdot \hat{c}_B \end{pmatrix}$$

This rotation matrix represents an axis-angle pair that will bring crystallite B into coincidence with crystallite A. It is convenient to express the axis of rotation and the misorientation angle in terms of a rotation matrix by the following relation

$$\theta = \cos^{-1}\left(\frac{g_{11} + g_{22} + g_{33} - 1}{2}\right)$$

$$v = \left(\frac{g_{23} - g_{32}}{2\sin\theta}, \frac{g_{31} - g_{13}}{2\sin\theta}, \frac{g_{12} - g_{21}}{2\sin\theta}\right) \quad (17)$$

We report this misorientation angle θ throughout this paper. We note that for small angles θ becomes ill-defined and the definition of the boundary axis becomes degenerate when $\theta \sim 0$.

Once we calculate the misorientation angle as a function of time during coalescence, the grain boundary misorientation decay time (τ_θ) is estimated by fitting θ in the form $\theta(t) = D + A\exp(-B(t - t_0))$, where *D*, *A*, *B*, and t_0 are the fitting parameters. In particular, the constant *B* determines the rate of GB diffusion; τ_θ is the time when θ changes to 5% of its initial value.

Finally, we evaluate the neck radius during crystallite coalescence by dividing the space between the centers of crystallites into concentric cylinders of finite width along an axis parallel to the line joining the centers. The radius at each point is determined by finding the minimum radius which consists of all the SNA of interest. In the initial stage, the radius has two maxima at the centers with a minimum at the center of the neck, as shown in the Supporting Information. As time passes, the convexity of the neck decreases and the radius is uniform, as seen in the Supporting Information. From these simulations, we extract the τ_{min} by calculating the time elapsed for the neck to grow to 80% of the initial crystallite radius.

Conflict of Interest: The authors declare no competing financial interest.

Acknowledgment. We thank Robert V. Kohn for insightful discussions and valuable suggestions. We also thank Ting Li for her careful reading of the manuscript. S.D. was supported by the Non-Equilibrium Energy Research Center (NERC) which is an Energy Frontier Research Center funded by the U.S. Department of Energy, Office of Science, Office of Basic Energy Sciences under Award Number DE-SC0000989, and K.L.K. was supported by the AFOSR MURI Grant FA9550-11-1-0275.

Supporting Information Available: Crystallite tracking algorithm, T_m calculation, misorientation angle (θ) definition, as well as animations showing temporal evolution of the bcc crystallite growth and the coalescence of two bcc grains. This material is available free of charge *via* the Internet at http://pubs.acs.org.

Note Added after Issue Publication: Two Supporting Information files were omitted from the version published November 26, 2013. The revised version with avi files was published on the Web February 19, 2014.

REFERENCES AND NOTES

1. Park, S. Y.; Lytton-Jean, A. K. R.; Lee, B.; Weigand, S.; Schatz, G. C.; Mirkin, C. A. DNA-Programmable Nanoparticle Crystallization. *Nature* **2008**, *451*, 553–556.
2. Wang, L. B.; Xu, L. G.; Kuang, H.; Xu, C. L.; Kotov, N. A. Dynamic Nanoparticle Assemblies. *Acc. Chem. Res.* **2012**, *45*, 1916–1926.
3. Miszta, K.; de Graaf, J.; Bertoni, G.; Dorfs, D.; Brescia, R.; Marras, S.; Ceseracciu, L.; Cingolani, R.; van Roij, R.; Dijkstra, M.; *et al.* Hierarchical Self-Assembly of Suspended Branched Colloidal Nanocrystals into Superlattice Structures. *Nat. Mater.* **2011**, *10*, 872–876.
4. Macfarlane, R. J.; Lee, B.; Jones, M. R.; Harris, N.; Schatz, G. C.; Mirkin, C. A. Nanoparticle Superlattice Engineering with DNA. *Science* **2011**, *334*, 204–208.
5. Xiong, H.; van der Lelie, D.; Gang, O. Phase Behavior of Nanoparticles Assembled by DNA Linkers. *Phys. Rev. Lett.* **2009**, *102*, 015504(1)–015504(4).
6. Auyeung, E.; Cutler, J. I.; Macfarlane, R. J.; Jones, M. R.; Wu, J. S.; Liu, G.; Zhang, K.; Osberg, K. D.; Mirkin, C. A. Synthetically Programmable Nanoparticle Superlattices Using a Hollow Three-Dimensional Spacer Approach. *Nat. Nanotechnol.* **2012**, *7*, 24–28.
7. Park, S.-J.; Lazarides, A.; Mirkin, C.; Brazis, P.; Kannewurf, C.; Letsinger, R. The Electrical Properties of Gold Nanoparticle Assemblies Linked by DNA. *Angew. Chem., Int. Ed.* **2000**, *39*, 3845–3848.
8. Schmid, G.; Simon, U. Gold Nanoparticles: Assembly and Electrical Properties in 1−3 Dimensions. *Chem. Commun.* **2005**, *0*, 697–710.
9. Storhoff, J. J.; Lazarides, A. A.; Mucic, R. C.; Mirkin, C. A.; Letsinger, R. L.; Schatz, G. C. What Controls the Optical

Properties of DNA-Linked Gold Nanoparticle Assemblies? *J. Am. Chem. Soc.* **2000**, *122*, 4640–4650.
10. Zhang, J.; Li, S.; Wu, J.; Schatz, G. C.; Mirkin, C. A. Plasmon-Mediated Synthesis of Silver Triangular Bipyramids. *Angew. Chem., Int. Ed.* **2009**, *48*, 7787–7791.
11. Payne, E. K.; Shuford, K. L.; Park, S.; Schatz, G. C.; Mirkin, C. A. Multipole Plasmon Resonances in Gold Nanorods. *J. Phys. Chem. B* **2006**, *110*, 2150–2154.
12. Hicks, E. M.; Zou, S.; Schatz, G. C.; Spears, K. G.; Van Duyne, R. P.; Gunnarsson, L.; Rindzevicius, T.; Kasemo, B.; Käll, M. Controlling Plasmon Line Shapes through Diffractive Coupling in Linear Arrays of Cylindrical Nanoparticles Fabricated by Electron Beam Lithography. *Nano Lett.* **2005**, *5*, 1065–1070.
13. Cong, T.; Wani, S. N.; Paynter, P. A.; Sureshkumar, R. Structure and Optical Properties of Self-Assembled Multicomponent Plasmonic Nanogels. *Appl. Phys. Lett.* **2011**, *99*, 043112(1)–043112(3).
14. Nehl, C. L.; Hafner, J. H. Shape-Dependent Plasmon Resonances of Gold Nanoparticles. *J. Mater. Chem.* **2008**, *18*, 2415–2419.
15. Fan, J. A.; He, Y.; Bao, K.; Wu, C.; Bao, J.; Schade, N. B.; Manoharan, V. N.; Shvets, G.; Nordlander, P.; Liu, D. R.; *et al.* DNA-Enabled Self-Assembly of Plasmonic Nanoclusters. *Nano Lett.* **2011**, *11*, 4859–4864.
16. Lee, K.-S.; El-Sayed, M. A. Gold and Silver Nanoparticles in Sensing and Imaging: Sensitivity of Plasmon Response to Size, Shape, and Metal Composition. *J. Phys. Chem. B* **2006**, *110*, 19220–19225.
17. Prigodich, A. E.; Seferos, D. S.; Massich, M. D.; Giljohann, D. A.; Lane, B. C.; Mirkin, C. A. Nano-Flares for mRNA Regulation and Detection. *ACS Nano* **2009**, *3*, 2147–2152.
18. Wang, T.; Zhuang, J.; Lynch, J.; Chu, O.; Wang, Z.; Wang, X.; LaMontagne, D.; Wu, H.; Wang, Z.; Cao, Y. C. Self-Assembled Colloidal Superparticles from Nanorods. *Science* **2012**, *338*, 358–363.
19. Macfarlane, R. J.; Lee, B.; Hill, H. D.; Senesi, A. J.; Seifert, S.; Mirkin, C. A. Assembly and Organization Processes in DNA-Directed Colloidal Crystallization. *Proc. Natl. Acad. Sci. U.S.A.* **2009**, *106*, 10493–10498.
20. Mirkin, C. A.; Letsinger, R. L.; Mucic, R. C.; Storhoff, J. J. A DNA-Based Method for Rationally Assembling Nanoparticles into Macroscopic Materials. *Nature* **1996**, *382*, 607–609.
21. Theodorakis, P. E.; Dellago, C.; Kahl, G. A Coarse-Grained Model for DNA-Functionalized Spherical Colloids, Revisited: Effective Pair Potential from Parallel Replica Simulations. *J. Chem. Phys.* **2013**, *138*, 025101(1)–025101(12).
22. Knorowski, C.; Burleigh, S.; Travesset, A. Dynamics and Statics of DNA-Programmable Nanoparticle Self-Assembly and Crystallization. *Phys. Rev. Lett.* **2011**, *106*, 215501(1)–215501(4).
23. Freeman, G. S.; Hinckley, D. M.; de Pablo, J. J. A Coarse-Grain Three-Site-per-Nucleotide Model for DNA with Explicit Ions. *J. Chem. Phys.* **2011**, *135*, 165104(1)–165104(13).
24. Zwanikken, J. W.; Guo, P.; Mirkin, C. A.; Olvera de la Cruz, M. Local Ionic Environment around Polyvalent Nucleic Acid-Functionalized Nanoparticles. *J. Phys. Chem. C* **2011**, *115*, 16368–16373.
25. Starr, F.; Francis, W. Sciortino Model for Assembly and Gelation of Four-Armed DNA Dendrimers. *J. Phys.: Condens. Matter* **2006**, *18*, L347–L353.
26. Padovan-Merhar, O.; Lara, F. V.; Starr, F. W. Stability of DNA-Linked Nanoparticle Crystals: Effect of Number of Strands, Core Size, and Rigidity of Strand Attachment. *J. Chem. Phys.* **2011**, *134*, 244701(1)–244701(7).
27. Dreyfus, R.; Leunissen, M. E.; Sha, R.; Tkachenko, A.; Seeman, N. C.; Pine, D. J.; Chaikin, P. M. Aggregation–Disaggregation Transition of DNA-Coated Colloids: Experiments and Theory. *Phys. Rev. E* **2010**, *81*, 041404(1)–041404(10).
28. Schall, P.; Cohen, I.; Weitz, D. A.; Spaepen, F. Visualizing Dislocation Nucleation by Indenting Colloidal Crystals. *Nature* **2006**, *440*, 319–323.
29. Frenkel, D. Colloidal Crystals: Plenty of Room at the Top. *Nat. Mater.* **2006**, *5*, 85–86.
30. Ishida, Y.; Ichinose, H.; Kizuka, T.; Suenaga, K. High-Resolution Electron Microscopy of Interfaces in Nanocrystalline Materials. *Nanostruct. Mater.* **1995**, *6*, 115–124.
31. Rengarajan, R.; Mittleman, D.; Rich, C.; Colvin, V. Effect of Disorder on the Optical Properties of Colloidal Crystals. *Phys. Rev. E* **2005**, *71*, 016615(1)–016615(11).
32. Van Swygenhoven, H.; Farkas, D.; Caro, A. Grain-Boundary Structures in Polycrystalline Metals at the Nanoscale. *Phys. Rev. B* **2000**, *62*, 831–838.
33. Zhang, W.; Schneibel, J. The Sintering of Two Particles by Surface and Grain Boundary Diffusion—A Two-Dimensional Numerical Study. *Acta Metall. Mater.* **1995**, *43*, 4377–4386.
34. Nagamanasa, K. H.; Gokhale, S.; Ganapathy, R.; Sood, A. K. Confined Glassy Dynamics at Grain Boundaries in Colloidal Crystals. *Proc. Natl. Acad. Sci. U.S.A.* **2011**, *108*, 11323–11326.
35. Biancaniello, P. L.; Kim, A. J.; Crocker, J. C. Colloidal Interactions and Self-Assembly Using DNA Hybridization. *Phys. Rev. Lett.* **2005**, *94*, 058302(1)–058302(4).
36. Varilly, P.; Angioletti-Uberti, S.; Mognetti, B. M.; Frenkel, D. A General Theory of DNA-Mediated and Other Valence-Limited Colloidal Interactions. *J. Chem. Phys.* **2012**, *137*, 094108(1)–094108(15).
37. Li, T. I.; Sknepnek, R.; Macfarlane, R. J.; Mirkin, C. A.; Olvera de la Cruz, M. Modeling the Crystallization of Spherical Nucleic Acid Nanoparticle Conjugates with Molecular Dynamics Simulations. *Nano Lett.* **2012**, *12*, 2509–2514.
38. Kohlstedt, K. L.; Olvera de la Cruz, M.; Schatz, G. C. Controlling Orientational Order in 1-D Assemblies of Multivalent Triangular Prisms. *J. Phys. Chem. Lett.* **2013**, *4*, 203–208.
39. Knorowski, C.; Travesset, A. Dynamics of DNA-Programmable Nanoparticle Crystallization: Gelation, Nucleation and Topological Defects. *Soft Matter* **2012**, *8*, 12053–12059.
40. Israelachvili, J. *Intermolecular and Surface Forces*, 2nd ed.; Academic Press: New York, 1991; pp 241–243.
41. Derjaguin, B. Untersuchungen über die Reibung und Adhäsion, IV. Theorie des Anhaftens kleiner Teilchen. *Kolloid Z.* **1934**, *69*, 155–164.
42. Asakura, S.; Oosawa, F. Interaction between Particles Suspended in Solutions of Macromolecules. *J. Polym. Sci.* **1958**, *33*, 183–192.
43. Steinhardt, P. J.; Nelson, D. R.; Ronchetti, M. Bond-Orientational Order in Liquids and Glasses. *Phys. Rev. B* **1983**, *28*, 784–805.
44. Sun, Y.; Harris, N. C.; Kiang, C.-H. The Reversible Phase Transition of DNA-Linked Colloidal Gold Assemblies. *Phys. A* **2005**, *354*, 1–9.
45. Ratke, L.; Voorhees, P. W. *Growth and Coarsening: Ostwald Ripening in Material Processing*; Springer: Berlin, 2002; pp 167–180.
46. Wert, C.; Zener, C. Interference of Growing Spherical Precipitate Particles. *J. Appl. Phys.* **1950**, *21*, 5–8.
47. Taylor, J.; Cahn, J.; Handwerker, C. I. Geometric Models of Crystal Growth. *Acta Metall. Mater.* **1992**, *40*, 1443–1474.
48. Taylor, J., II. Mean Curvature and Weighted Mean Curvature. *Acta Metall. Mater.* **1992**, *40*, 1475–1485.
49. Wulff, G. On the Question of the Rate of Growth and Dissolution of Crystal Surfaces. *Z. Kristallogr. Mineral.* **1901**, *34*, 449–530.
50. Humphrey, W.; Dalke, A.; Schulten, K. VMD: Visual Molecular Dynamics. *J. Mol. Graphics* **1996**, *14*, 33–38.
51. Rupich, S. M.; Shevchenko, E. V.; Bodnarchuk, M. I.; Lee, B.; Talapin, D. V. Size-Dependent Multiple Twinning in Nanocrystal Superlattices. *J. Am. Chem. Soc.* **2010**, *132*, 289–296.
52. Thompson, C. V. Structure Evolution during Processing of Polycrystalline Films. *Annu. Rev. Mater. Sci.* **2000**, *30*, 159–190.
53. Mackenzie, J. K. Second Paper on Statistics Associated with the Random Disorientation of Cubes. *Biometrika* **1958**, *45*, 229–240.

54. Leite, E. R.; Giraldi, T. R.; Pontes, F. M.; Longo, E.; Beltran, A.; Andres, J. Crystal Growth in Colloidal Tin Oxide Nanocrystals Induced by Coalescence at Room Temperature. *Appl. Phys. Lett.* **2003**, *83*, 1566–1568.
55. Moore, L. J.; Dear, R. D.; Summers, M. D.; Dullens, R. P. A.; Ritchie, G. A. D. Direct Observation of Grain Rotation-Induced Grain Coalescence in Two-Dimensional Colloidal Crystals. *Nano Lett.* **2010**, *10*, 4266–4272.
56. Moldovan, D.; Yamakov, V.; Wolf, D.; Phillpot, S. R. Scaling Behavior of Grain-Rotation-Induced Grain Growth. *Phys. Rev. Lett.* **2002**, *89*, 206101(1)–206101(4).
57. Olvera de la Cruz, M.; Mayes, A. M.; Swift, B. W. Transition to Lamellar-Catenoid Structure in Block-Copolymer Melts. *Macromolecules* **1992**, *25*, 944–948.
58. Sknepnek, R.; Anderson, J. A.; Lamm, M. H.; Schmalian, J.; Travesset, A. Nanoparticle Ordering *via* Functionalized Block Copolymers in Solution. *ACS Nano* **2008**, *2*, 1259–1265.
59. Auyeung, E.; Li, T. I. N. G.; Senesi, A. J.; Schmucker, A. L.; Pals, B. C.; Olvera de la Cruz, M.; Mirkin, C. A. Wulff Polyhedra from DNA-Interconnected Particle Superlattices. *Nature*, in press.
60. Plimpton, S. Fast parallel algorithms for short-range molecular dynamics. *J. Comput. Phys*. **1995**, *117*, 1−19. (http://lammps.sandia.gov/).
61. Martinez, L.; Andrade, R.; Birgin, E. G.; Martinez, J. M. PACKMOL: A Package for Building Initial Configurations for Molecular Dynamics Simulations. *J. Comput. Chem.* **2009**, *30*, 2157–2164.